Developing a novel high-strength Al-Mg-Zn-Si alloy for laser powder bed fusion

Feipeng Yang [a], Jianying Wang [a], Tao Wen [a], Lei Zhang [a], Xixi Dong [b], Dong Qiu [c], Hailin Yang [a,*], Shouxun Ji [b]

a. State Key Laboratory of Powder Metallurgy, Central South University, Changsha 410083, China

b. Brunel Centre for Advanced Solidification Technology (BCAST), Brunel University London, Uxbridge, Middlesex, UB8 3PH, United Kingdom

c. Centre for Additive Manufacturing, School of Engineering, RMIT University, Melbourne, VIC 3000, Australia

* Corresponding authors: y-hailin@csu.edu.cn

Abstract: Additively manufactured (AM) aluminium alloys have attracted increasing attention due to the great demand of prototyping, spare parts supply, short run productions and further light-weighting of vehicles. However, most of the reported AM aluminium alloys are usually modified version of commercial cast or wrought alloys. In this work, we successfully developed a new high-strength and ductile Al5Mg3Zn2Si alloy, which is designed for laser powder bed fusion (LPBF) process. The optimised relative density of 98.9% was obtained at a volumetric energy density (VED) of 129.1 J/mm^3. The as-LPBFed Al5Mg3Zn2Si alloy features refined equiaxed α-Al grains and Al-Mg_2Si eutectic network. In addition, the sub-micrometre sized, coherent α-Al(Fe,Mn)Si and $MgZn_2$ dispersoids in conjunction with high number density of (Mg,Zn)-rich GP zones co-contribution to the excellent combination of mechanical properties, i.e. the ultimate tensile strength of 548 MPa, the yield strength of 403 MPa, and the elongation of 6.7%. The synergy of high strength and ductility results from the unique strengthening mechanisms provided by the combination of high cooling rate from LPBF and the typical composition in the aluminium alloy.

Key words: Aluminium alloys; Microstructure; Mechanical property; Additive manufacturing; Laser powder bed fusion

1. Introduction

Aluminium (Al) alloys have been widely used as structural materials in transportation sector due to their low density, high specific strength and low cost [1]. Currently, Al alloys are commonly manufactured by conventional techniques such as casting, welding, forging, extrusion, stamping and powder metallurgy, to satisfy the applications in a variety of engineering sectors. However, these manufacturing processes feature long lead time and limited flexibility of structural design. In contrast, laser powder bed fusion (LPBF) is an emerging metal additive manufacturing (AM) technology, which enables greater design flexibility for complex geometry and significantly reduces the tooling cost, materials waste and shortens the lead time for low volume production [2, 3]. In addition, the rapid solidification induced by the high cooling rate during LPBF process promotes the formation of refined microstructures with supersaturated solid solution and uniformly dispersed secondary phases [4-6], which is usually beneficial to improve the mechanical properties of alloys. However, due to the low laser absorptivity, high oxygen affinity, it has been challenging to manufacture sound components made of Al alloys by LPBF [7]. Metallurgical defects including hot cracking, inclusions and porosity are major concerns the LPBF process of Al alloys, in particular those with a large solidification range, like Al-Cu (2xxx), Al-Mg-Si (6xxx) and Al-Mg-Zn-Cu (7xxx) alloys [8]. Therefore, the development of new Al alloys that are highly compatible with the LPBF process and make the full use of LPBF's characteristics to improve mechanical properties has become a hot research topic in the last decade.

Generally, the development of new Al alloys for the LPBF process can be divided into two categories. The first strategy is to modify the commercial alloys by adding special trace elements or nanoparticles. For example, an Al-Mn (3xxx) alloy was modified using Sc and Zr and reached a good yield strength (YS) (438 ± 3 MPa) and a high elongation (El) (19 ± 3%) [9]. Similar studies for Zr/Sc-modified Al-Li [10], Al-Cu [11], Al-Mg [12], Al-Mg-Si [13, 14] and Al-Zn-Mg-Cu [15] alloys processed by LPBF, also showed a combination of high strength and elongation. Moreover, Martin et al. [8] decorated AA7075 alloy powder by adding nano-ZrH_2 particles as grain refiner, to minimize the tendency of hot tearing during the LPBF process, and the ultimate tensile strength (UTS) reached 383~417 MPa with the El of 3.8~5.4%. Recently, Li et al. [16] found that Ta nanoparticle enhanced LPBFed Al-Zn-Mg-Cu alloys to increase the UTS to 401 ± 11 MPa with the El of 5.1 ± 0.6%. Also, Xiao et al. [17] founded that Nb nanoparticle enabled grain refinement in an Al-Zn-Mg-Cu alloy, which obtained crack-free LPBFed samples with the UTS of ~ 505 ± 12 MPa. The second strategy is to design

new alloy system with short solidification range to reduce the hot-tearing susceptibility. Yang et al. [18] processed a new Al-5Mg-2Si alloy by LPBF to offer the UTS of 452 ±11 MPa and the El of 9.3 ±2.5% under as-fabricated condition. Deng et al. [19] processed a novel Al-5.7Ni alloy by LPBF, and the UTS and El were 407 MPa and 9.5%, respectively. Other alloys such as Al-Fe [20], Al-Ce-Mg [21] and Al-Ce-Mn [22] were also fabricated successfully by using LPBF and showed the combination of high strength and good processibility.

In our previous work, the LPBFed Al-5Mg-2Si alloy has demonstrated promising mechanical properties and excellent processability. Based on this early success, further alloy development was undertaken through zinc addition. It is well recognised that (Mg, Zn)-rich precipitates (which might stay in multiple meta-stable phases) are the prominent contributors of the high strength of Al-Zn-Mg-Cu (7xxx) alloys. Therefore, it is expected that addition of Zn into this Al-5Mg-2Si alloy could further enhance the mechanical properties through additional precipitation strengthening during the intrinsic thermal cycles. To test this hypothesis, we modified Al-5Mg-2Si alloy with 3wt% Zn addition and fabricated a new Al-5Mg-3Zn-2Si alloy by LPBF in this work. The processing window, phase constituents, microstructure at different length scales and tensile properties of this new Al alloy were comprehensively characterized. The low hot-tearing susceptibility and fine equiaxed grains in the as-fabricated Al-5Mg-3Zn-2Si alloy were explained and the contribution of each strengthening mechanism in to the overall yield strength was also discussed.

2. Experimental

2.1. Pre-alloyed powder preparation

Al5Mg3Zn2Si alloy powders were prepared by gas atomization, and argon (99.9%) was used as protective atmosphere to prevent powder oxidation during process. The detailed composition of the alloy powders was measured via inductively coupled plasma atomic emission spectrometry (ICP-AES) and the results are presented in Table 1. The morphology, size and microstructure of the atomized Al5Mg3Zn2Si alloy powders are shown in Fig. 1. It is seen that the particle size ranges from 12.2 to 82.7 μm with the mean size of 39.8 μm(Fig. 1b), measured by a laser particle size analyser (Matersizer). And the cross-section of particles in Figs. 1c and 1d exhibited the primary α-Al grains and eutectic network. The dendritic arm spacing is at a level of 1 μm in the powder particles in the as-received powder.
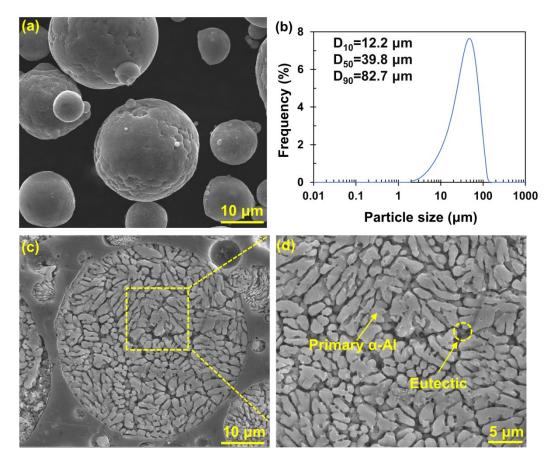
Fig. 1. (a) SEM micrograph showing the morphology of Al5Mg3Zn2Si alloy powder particles, (b) distribution of particle size, (c) and (d) SEM micrographs showing the microstructure of a particle on the cross-section of Al5Mg3Zn2Si alloy.

Table 1 The composition of experimental alloy powder calibrated by ICP-AES (wt.%).

Alloy	Mg	Zn	Si	Mn	Fe	Al
Al5Mg3Zn2Si	5.39	3.08	1.96	0.75	0.17	Balance

2.2. LPBF fabrication process

The LPBF process was conducted using a FS271M system (Farsoon, Inc, China). In detail, the system was powered by a 500 W fibre laser at a laser beam size of 90 μm. During the LPBF process, the printing chamber was filled with high purity argon to avoid oxygen contamination. The LPBFed samples were manufactured on a plate of AA6061 Al alloy.
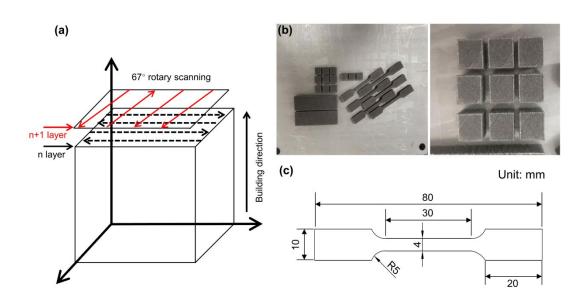
Fig. 2. (a) Schematic of laser beam scanning during sample fabrication, (b) optical micrograph showing the tensile samples and cubic samples obtained from optimized parameters, and (c) the dimension of tensile test sample.

The scanning track of laser beam is schematically shown in Fig. 2a, in which laser scanning was rotated by 67° between the adjacent layers. The cubic samples had a dimension of 10 mm × 10 mm ×10 mm (Fig. 2b). The tensile samples with the dimension of 80 mm × 10 mm × 2 mm were machined from LPBFed block, as shown in Fig. 2c. The optimized processing parameters included the hatch spacing (h) at 0.1 mm, layer thickness (t) of 0.03 mm, laser power (P) of 270, 310, 350 W, scan speed (v) of 600, 800, 1000, 1200, and 1400 mm/s. Those parameters were selected to process Al5Mg3Zn2Si samples, which were based on our previous study about Al5Mg2Si alloy [18]. The LPBFed samples were mechanically ground and polished to reach the same surface condition for further characterizations.

2.3. Microstructure characterization

The Archimedes method was used to evaluate the relative density of LPBFed samples. The surface defects of samples were characterized by Leica DM4000M optical microscope. Phase constituent and crystal structure of the powder and LPBFed alloys were examined by X-ray diffraction technique with Cu Ka radiation (XRD, Rigaku). The microstructures were characterized by FEI nano230 field emission scanning election microscope (FE-SEM), and the samples were etched using Keller's solution before SEM characterization. The grain size and orientation angle distribution were observed in a FIB Helios NanoLab G3 UC system equipped with a Hikari camera and the TSL OIM data analysis software for EBSD. Before EBSD characterization, the

samples were finished by electrochemical polishing for 12 s at 20 V in a corrosive solution of CH_3OH and HNO_3. Furthermore, the transmission electron microscope (TEM:Tecnai G2 F20) was used microstructure characterization at a sub-micrometer scale. And the TEM samples were prepared using the precision ion polishing system (PIPS). And the average diameter and volume fraction of the particles are calculated by Image-Pro Plus with high angle annular dark field (HAADF) TEM images.

2.4. Mechanical properties testing

Dog-bone-shaped tensile samples shown in Fig. 2c were cut by electrical discharge machining. The surface of gauge length of each specimen was finished using a 2000 grit SiC paper. The tensile tests were conducted on MTS Alliance RT30 detecting system with a strain rate of 1×10^{-3} s^{-1}. The micro-hardness was measured by a micro-Vickers hardness tester under a load of 200 g for 15 s (ASTME 384-08), and the micro-hardness values were averaged of from 10 different areas on the same surface.

3. Results

3.1. Processing windows for LPBF

The relative density of as-fabricated samples is usually used to evaluate the processability of a given alloy during LPBF [23, 24]. The process parameters, relative density and mechanical properties of as-fabricated alloys are closely linked with the volumetric energy density (VED), which can be described as [25]: VED=P/vht. Fig. 3(a) shows the relation between VED and the relative density of LPBFed Al5Mg3Zn2Si alloy. The density increased initially at the VED range of 62-107 J/mm^3, then formed a parabolic plateau at the VED range of 107-129.1 J/mm^3 and followed by a decrease at the VED range of 129.1-157.1 J/mm^3. The maximum density of 98.9% was obtained at the VED of 129.1 J/mm^3, suggesting the good processability of the Al5Mg3Zn2Si alloy. In contrast, lower or higher levels failed to make sound samples because of the high level of defects. Meanwhile, the hardness of LPBFed alloys at different VEDs is presented in Fig. 3(b). It is found that the harndess slightly incleased with the increasing VEDs, then reached the peak at the VED of 129 J/mm^3 followed by a gradual decrease at higher VED levels. Moreover, the higher hardness was observed perpendicular to build direction than build direction at all VED levels. Correspondingly, optical micrographs (OM) of the horizontal cross-sections are shown in Fig. 3(c). It could be observed that an insufficient laser energy causes the lack of fusion and some unmelted particles. With increasing VEDs, the powder are completely melted to liquid phase,

leading to a smooth flow and diffuse of the liquid in the molten pool. In this case, the samples present only a few gas pores and achieve a high relative density. However, when the VED exceeds 129.1 J/mm^3, the key-hole mode melting is formed, in which the relative density of the sample is apparently reduced. Overall, the results of relative density, hardness and optical micrographs of LPBFed alloy confirmed the optimized processing parameters as v of 800 mm/s, P of 310 W, and VED of 129.1 J/mm^3. Due to the nearly full density and higher hardness, the typical microstructures are observed using LPBFed Al5Mg3Zn2Si sample made with optimal process parameters.
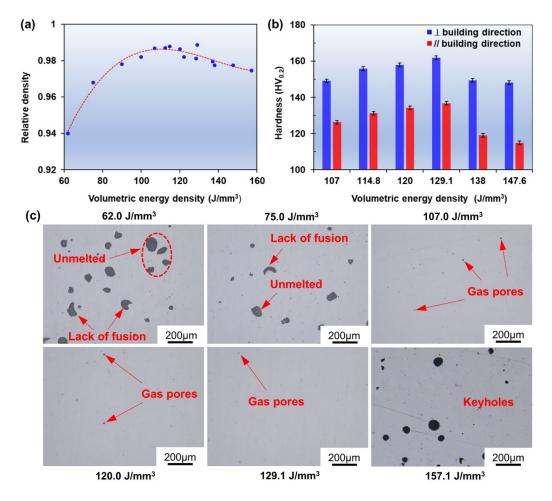

Fig. 3. (a) The density of LPBFed Al5Mg3Zn2Si samples obtained at different volumetric energy density, (b) the micro-hardness versus volumetric energy density, (c) optical micrographs (OM) from the horizontal cross-sections of the as-built Al5Mg3Zn2Si alloy.

3.2. Phase constituents analysis

Fig. 4 shows the XRD spectra of the Al5Mg3Zn2Si alloy in the powder and LPBFed condition. α-Al phases and Mg$_2$Si phases were clearly visible, but MgZn$_2$ phase was weak in the powder and LPBFed samples. The disappearance of Mn-containing phase and very weak MgZn$_2$ peak phase were probably related to the low Mn content and high

cooling rate to increase the solubility of element in the matrix respectively. From the XRD results of LPBFed sample and powder in Fig. 4(b), the diffraction peaks of α-Al at same grain orientation presented different intensity, which may mean that the preferential grains orientations of LPBFed sample is changed compared to that of the powder [26, 27]. Moreover, the diffraction peaks of α-Al showed a slight shift to high angles, indicating a slight decrease of the lattice constant of α-Al (see Fig. 4b), On the other hand, a large amount of thermal stress accumulated inside the LPBFed alloy due to rapid solidification process at high cooling rate, which makes the crystal lattice of the printed sample distorted [28, 29]. Also, the decomposition of the supersaturated solid solution may further promote the lattice distortion during the LPBF process [30].
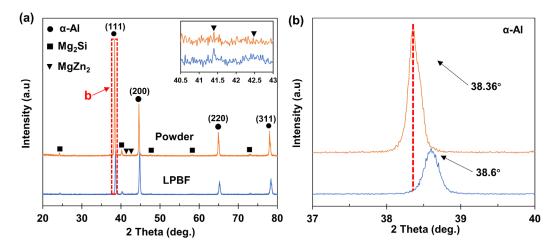

Fig. 4. The XRD spectra for the phase analysis in the powder and LPBFed Al5Mg3Zn2Si samples, (a) overall spectra, the inset shows magnified XRD spectra of 40.5° to 43° in (a), and (b) detailed from 38° to 39°.

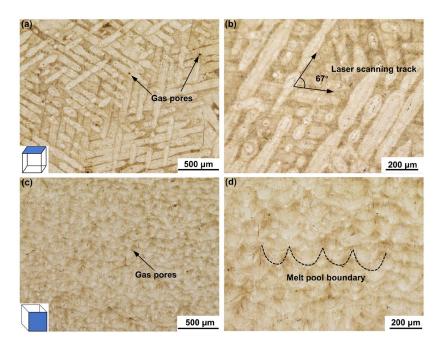## 3.3. Refinement in as-fabricated microstructure

Fig. 5. OM micrographs showing the microstructure of the LPBFed Al5Mg3Zn2Si alloy at VED of 129.1 J/mm³, on the (a, b) horizontal section and (c, d) longitudinal section.

Fig. 5 shows the etched microstructure of the as-fabricated samples at the VED of 129.1 J/mm³. In the horizontal section, continuous laser tracks with an angel of 67° were presented in Fig. 5a&b, and the melt pool boundaries were clearly observed on the longitudinal section (Fig. 5c&d). Meanwhile, the gas porosities were formed in two sides, which were consistent with the results obtained in Fig. 3c. Further investigation in SEM (Figs. 6a-f) exposed the typical microstructure in the as-LPBFed Al5Mg3Zn2Si alloy along different directions. The typical microstructure could be divided into coarse grain zone (CG), heat affected zone (HAZ) and fine grain zone (FG) in both directions. Unlike the microstructure of as-cast Al-Mg-Si alloy where large rod-like or lamellar-like Mg_2Si particles precipitated in the Al matrix [31], cellular eutectic microstructures with nanosized Mg_2Si particles were formed in the as-LPBFed Al5Mg3Zn2ZSi alloy. Meanwhile, Similar eutectic structures were also founded in as-LPBFed Al-Si alloys [32-35]. And the nanosized eutectic structures were characterized by a light α-Al matrix decorated with dark Mg_2Si network. It is founded that numerous equiaxed eutectic cells were homogenously distributed in the horizontal direction (Figs. 6(a-c)). And the equiaxed cells were typically presented on the average size of 0.84 μm in CG (Fig. 6a), and 0.26 μm in FG (Fig. 6b&c). Inside the HAZ, the cellular Mg_2Si network was presented as irregular particles. The microstructure on the longitudinal section is shown in Figs. 6(d-f). In Fig. 6d, the primary grains composed of equiaxed and columnar eutectic cell on the longitudinal section. And the equiaxed eutectic cell was observed in

the CG with an average size of 0.95 μm (Fig. 6d). However, the equiaxed and columnar eutectic cells appeared in the FG (Figs. 6e&f). The average size of equiaxed eutectic cell was 0.38 μm, and the size of columnar eutectic cell was a few microns long and at a level of 0.4~0.5 μm wide. The typical feature in the different directions is that the three grain zones existed in the whole direction, However, the difference reflected in microstructure was that only equiaxed eutectic cells were appeared on the horizontal direction, but equiaxed and columnar eutectic cell on the longitudinal section.
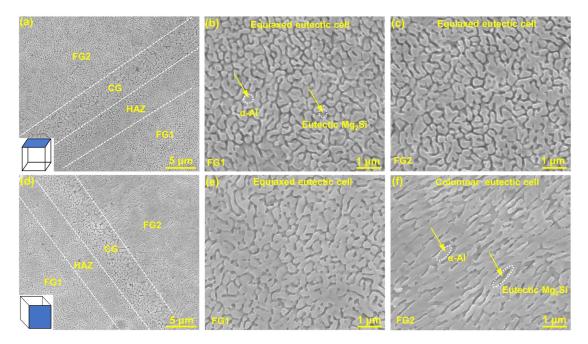

Fig. 6. SEM micrographs showing the microstructure of the LPBFed Al5Mg3Zn2Si alloy, (a) the overall microstructure, (b) equiaxed eutectic cells in fine grain zone 1, and (c) equiaxed eutectic cells in fine grain zone 2 on horizontal section, (d) the overall microstructure, (e) equiaxed eutectic cells in fine grain zone 1, (f) columnar eutectic cells in fine grain zone 2 on the longitudinal section.

The inverse pole figures (IPFs) in Figs. 7a and 7b showed the grain orientation and size distribution detected from the horizontal and longitudinal cross-section, respectively. From the IPFs map, it is obvious that the numerous equiaxed grains were observed on the horizontal section. And the equiaxed-columnar bimodal grain structure clearly distributed along the temperature gradient direction of melt pool on the longitudinal cross-section. Correspondingly, the distribution of grain aspect ratio on two cross-sections is presented in Figs. 7c and 7d, respectively. For clarity, the aspect ratio is defined as the ratio of width to length. Accordingly, the grains with aspect ratio less than 0.5 is classified as columnar grains while the ones with aspect ratio between 0.5 and 1 are regarded as equiaxed grains. It is founded that there were more equiaxed grains in the horizontal cross-section compared to the longitudinal cross-section. The

grain sizes were mainly in the range of 7~25 μm, as indicated in Figs. 7e and f. The average grain sizes on the horizontal and longitudinal section were 13.1 μm and 14.4 μm, respectively. From the orientation angle distribution on the horizontal and longitudinal section in Figs. 7g and 7h, it is found that the orientation angle distribution of LPBFed samples was selective orientation, and the fraction of low-angle grain boundary (LAGB, <15º) were 54.7% and 45.3% in the horizontal and longitudinal section, respectively. Apparently, there was a higher proportion of LAGBs on as-LPBFed samples, which could be beneficial to improve the strength of fabricated parts [36].
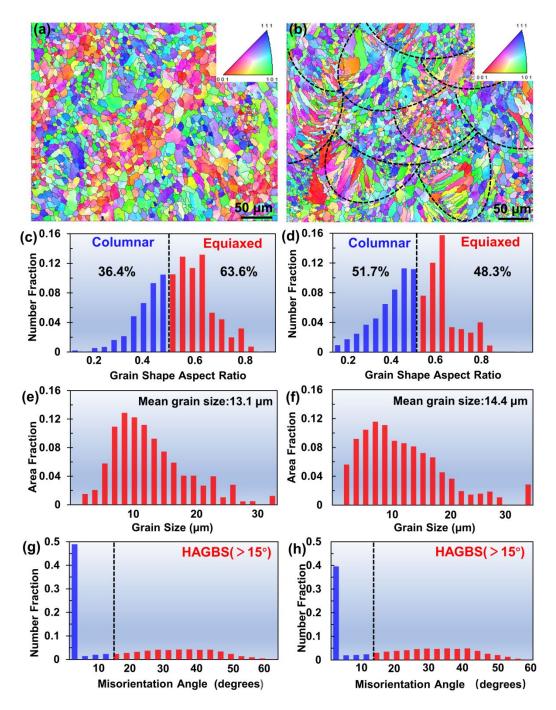
Fig. 7. The inversed pole figure (IPF) on (a) horizontal cross-section and (b) cross-section, the grain shape aspect ratio on (c) horizontal cross-section and (d) longitudinal cross-section, the grain size distribution on (e) horizontal cross-section and (f) longitudinal cross-section, and the grain boundary orientation angle distribution on (g) horizontal cross-section and (h) longitudinal cross-section of the LPBFed Al5Mg3Zn2Si alloy.

To better characterize the microstructure in sub-micrometre levels, TEM-EDS analysis was undertaken and the results are shown in Fig. 8. The typical structures in as-LPBFed sample (Figs. 8a and 8b) consisted of columnar and equiaxed eutectic cells. Meanwhile, the dislocations were also observed in the side of eutectic cells and secondary phases were uniformly distributed in the eutectic cells. HAADF-STEM image is shown in Fig. 8c for detailed eutectic cells and the corresponding elemental distribution is presented in Fig. 8d. Firstly, both Mg and Si were enriched at the same local areas along the cellular boundaries, which manifested that these (Mg, Si) enriched particles were divorced Al-Mg_2Si eutectics. Also, the distribution of Mn and Fe were also highly correlated next to the eutectics, and such (Mn, Fe)-rich globular particles with a size of 20-30 nm were likely to be α-AlFeMnSi phase. Moreover, numerous rod-like (Mg, Zn)-rich particles inside the α-Al grain were 30-60 nm long and 5 nm wide, indicating that these particles were likely to be (Mg, Zn)-rich precipitates. The detailed morphology and compositions of particles distributed inside α-Al grains and at the cellular boundaries are shown in Fig. S1.
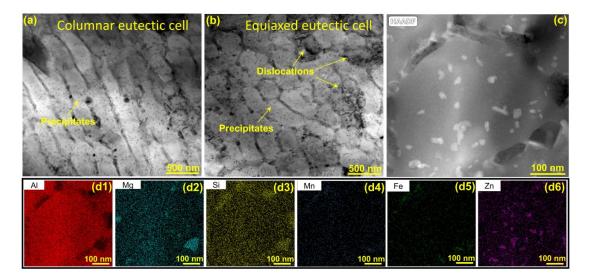

Fig. 8. TEM micrographs showing the microstructure and elemental distributions of the LPBFed Al5Mg3Zn2Si alloy, (a) columnar eutectic cell, (b) equiaxed eutectic cell, (c) HAADF-STEM image showing the cellular structure, and (d) corresponding mapping of main elements of Al, Mg, Si, Mn, Fe and Zn.

To further verify the identity of each secondary phase, the HRTEM images and SAED patterns of each type of secondary phase are shown in Fig. 9. The indexed SAEDs confirmed that the secondary phases were Mg_2Si, α-Al(Fe,Mn)Si and $MgZn_2$ respectively. The interface between α-Al and Mg_2Si phase was observed in Fig. 9a, and the corresponding diffraction pattern images from two phases are shown in insert. By indexing the diffraction patterns, two diffraction patterns were founded corresponding to [011] zone axis of the α-Al and $[\bar{1}12]$ zone axis of the Mg_2Si phase respectively. It is indicated that the $(\bar{2}00)$ plane of α-Al is parallel to the $(1\bar{1}1)$ plane of Mg_2Si from the diffraction patterns. This suggests that the interface could be semi-coherent. And the orientation relationships of the two phases could be expressed as $(\bar{2}00)_{Al}$ // $(1\bar{1}1)_{Mg2Si}$, $[011]_{Al}$ // $[\bar{1}12]_{Mg2Si}$. In addition, Fig. 9b shows the HRTEM image of the interface between α-Al and α-AlFeMnSi phase. From the corresponding FFT pattern (Fig. 9b), it indicates that the α-AlFeMnSi has a body-centred cubic structure. Meanwhile, the α-Al was viewed along the $[011]_{Al}$ direction, while the α-Al(Fe,Mn)Si was aligned along the $[\bar{1}22]_{α\text{-AlFeMnSi}}$ direction. The $(\bar{1}1\bar{1})_{Al}$ and $(1\bar{1}1)_{Al}$ plane from α-Al phase are almost parallel to the $(110)_{α\text{-AlFeMnSi}}$ and $(110)_{α\text{-AlFeMnSi}}$ plane respectively. Therefore, the orientation relationships between α-Al(Fe,Mn)Si phase and α-Al were described as $(\bar{1}1\bar{1})_{Al}$ // $(0\bar{2}2)_{α\text{-AlFeMnSi}}$, $(1\bar{1}1)_{Al}$//$(420)_{α\text{-AlFeMnSi}}$ and $[011]_{Al}$//$[\bar{1}22]_{α\text{-AlFeMnSi}}$, indicating that the α-Al(Fe,Mn)Si phase was semi-coherent with the α-Al. The interface between α-Al and $MgZn_2$ phase is presented in Fig. 9c. It identified that the beam direction was parallel to $[011]_{Al}$ and $[10\bar{1}0]_{MgZn2}$. Meanwhile, the diffraction spots including $(\bar{1}1\bar{1})_{Al}$ and $(000\bar{2})_{MgZn2}$ were aligned in a straight line, furthermore, indicating a semi-coherent interface between two phases. And this orientation relationship could be expressed as $(\bar{1}1\bar{1})_{Al}$ // $(000\bar{2})_{MgZn2}$, $[011]_{Al}$ // $[10\bar{1}0]_{MgZn2}$. Meanwhile, high-density plate-shaped particles were observed inside divorced Al-Mg_2Si eutectics as shown in Fig. 9d, with 20-30 nm in length and about 3 nm in width. the string-like diffraction patterns in Fig. 9f&g indicated that these particles were most likely the (Mg, Zn)-rich G-P zones. Well-developed orientation relationships were observed between individual precipitate and α-Al matrix based on the SAED patterns. It is suspected that the fine precipitate might promote the formation of dislocation loop due to the good interface relationship between the α-Al and the precipitate, leading to Orowan strengthening mechanism and hence higher strength [37].
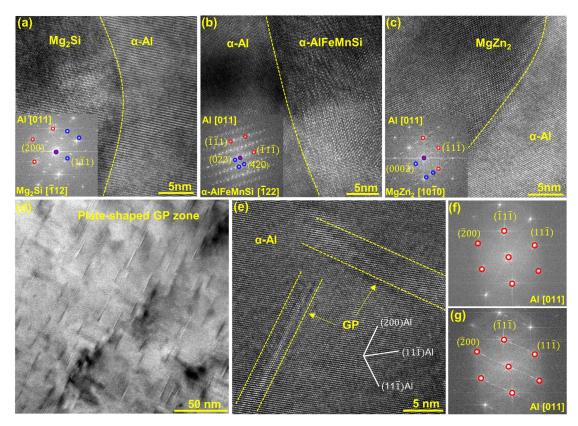
Fig. 9. HRTEM micrographs and corresponding SAED patterns showing (a) Mg_2Si, (b) α-Al(Fe,Mn)Si and (c) $MgZn_2$ phases, (d) high number density plate-shaped GP zones inside Al-Mg_2Si eutectic, (e) HRTEM image of GP zones and (f), (g) the SAED patters of GP zones.

3.4. Mechanical properties

The typical tensile stress-strain curves of LPBFed Al5Mg3Zn2Si alloys at different VEDs are shown in Fig. 10a and the numerical data are presented in Table 2. The selected reference values were obtained from the as-LPBFed Al alloy samples processed perpendicular to building direction. It is noted that the UTS and YS showed a positive correlation with the VED in the range of 107-129.1 J/mm^3. When the VED was 129.1 J/mm^3, both the UTS and the YS reached the peak values of 548 MPa and 403 MPa, respectively, with a moderate El of 6.7% under as-fabricated condition. Further increasing the VED value beyond 129.1 J/mm^3, the UTS and YS were weakened. Fig. 10b summarized the UTS and El of a variety of Al alloys fabricated by different techniques, including our previous study on as-LPBFed Al-5Mg-2Si alloy [18], Al-Si alloy [32, 38-47], Al-Mg-Si-Sc/Zr alloy [13, 14], Al-Zn-Mg-Cu-Sc/Zr alloy [8, 48, 49] under as-LPBFed condition, Al-Mg-Si alloy under as-cast condition [31, 50-56] and the as-LPBFed Al5Mg3Zn2Si alloy in this work. The high UTS value of 548 MPa enabled the as-LPBFed Al5Mg3Zn2Si alloy a clear advantage over commonly

used Al-Si based alloys. The as-LPBFed Al5Mg3Zn2Si alloy also demonstrated a great potential to compete with Sc/Zr modified as-LPBFed Al-Zn-Mg-Cu-Sc-Zr alloys because the same level of UTS could be achieved in the absence of costly alloying elements, i.e Sc/Zr. The features on the fractured surface after tensile testing are shown in Figs. 10c and 10d. A large portion of local areas with very fine dimples (< 1μm) were observed. Such a feature of ductile fractures was consistent with the moderate elongation in the as-LPBFed Al5Mg3Zn2Si alloy.
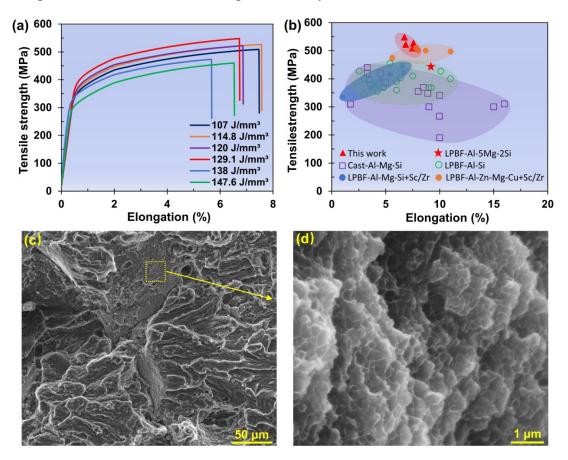

Fig. 10. (a) Stress-strain curves of the as-LPBFed Al5Mg3Zn2Si samples at different VEDs, (b) the UTS obtained by the as-LPBFed Al5Mg3Zn2Si samples and the comparison of UTS between the alloy in this study and other Al alloys reported in literatures. (c) the fractography of the as-LPBFed Al5Mg3Zn2Si simple processed at VED of 129.1 J/mm^3 and (d) the detailed dimples in the fractured surface.

Table 2 The ultimate tensile strength (UTS), yield strength (YS) and elongation (El) of the as-LPBFed Al5Mg3Zn2Si alloy processed at different VEDs.

VED (J/mm^3)	107	114.8	120	129.1	138	147.6
UTS (MPa)	509±2	522±3	527±5	548±6	473±8	460±5
YS (MPa)	360±3	374±4	382±4	403±4	337±7	312±2
El (%)	7.5±0.3	7.6±0.5	6.9±0.4	6.7±0.3	5.7±0.2	6.5±0.2

4. Discussion

4.1. The processability of Al5Mg3Zn2Si alloy

Our previous study on the as-LPBFed Al-5Mg-2Si alloy showed excellent processability, which was attributed to the narrow solidification range [18]. In general, the addition of Zn might increase the hot-cracking susceptibility of Al alloy [57, 58]. However, in this work, no hot cracks were observed in the as-LPBFed Al5Mg3Zn2Si alloy when the VED was set in the range of 107-129.1 J/mm^3 (see Fig. 3c). Generally, the as-LPBFed Al alloy samples are prone to form cracking because of the high cooling rate and sharp thermal gradient in LPBF process and the large solidification range [7]. On the one hand, a large amount of thermal stress is accumulated inside the as-LPBFed alloy due to rapid solidification process at high cooling rates. Once stress concentration exceeds the strength limit of the material, the cracking occurs. The specific thermal stress value is difficult to accurately measure during the rapid solidification process. But it has been proved that thermal stress can be eliminated to a certain extent using suitable scanning strategy and pre-heating temperature [14, 24]. This method was also adopted to mitigate the crack initiation in this study. The low hot-cracking susceptibility of the as-LPBFed Al5Mg3Zn2Si alloy can be mainly attributed to the following factors.

Firstly, the refined eutectics helps to reduce solidification cracking. For the as-LPBFed Al5Mg3Zn2Si alloy, numerous Al-Mg$_2$Si fine eutectic cells with the diameter of 300~400 nm were observed (Fig. 8). This is extremely beneficial for the mitigation of hot-cracking. Due to the low melting point and the good flowability, the formation of Al-Mg$_2$Si eutectic helps to mitigate hot-cracking by eutectic feeding during solidification. Similar cases can be seen in Al-Si alloys such as AlSi10Mg [32], AlSi7 [44] and AlSi12 [45].

Secondly, the equilibrium phase diagram of Al5Mg3Zn2Si-xZn alloys on the cross section of Al-5.39Mg-1.96Si-0.75Mn was presented in Fig. 11. It is found that primary α-Al$_{15}$(Fe,Mn)$_3$Si$_2$ phase should form as a prior phase during solidification. From the microstructure shown in Fig. 8 and Fig. S1, the primary α-AlFeMnSi nanoparticles are distributed along the cellular boundaries, which may promote the formation of fine equiaxed grains resulted from particle pinning effect [59, 60]. This explains why 48.3% of the primary grains are equiaxed on the longitudinal cross-section. Compared with the coarse columnar grains, the fine equiaxed grains are easier to accommodate thermal strains, therefore suppressing the coherency between adjacent grains [8]. Also, more interfaces in the fine equiaxed grains are capable of disrupting the thermal stress and improving the liquid feeding during solidification process [61]. Additionally, in

contrast to the flat interfaces between coarse columnar grains, the crack paths become more tortuous in the fine equiaxed grains, and hence the crack propagation is effectively restrained [62]. As such, the enhanced formation of fine equiaxed grain structure can greatly prevent the formation of hot cracking, resulting in a satisfied formability for the Al5Mg3Zn2Si alloy.
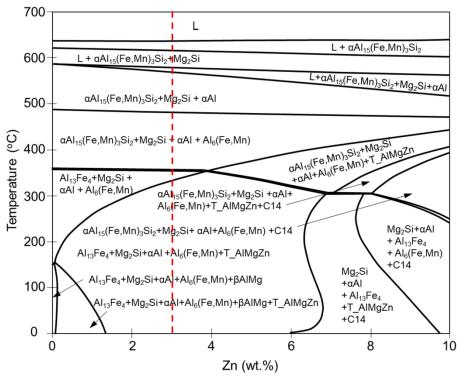

Fig. 11. The equilibrium phase diagram of Al5Mg3Zn2Si-xZn alloys on the cross section of the Al-5.39Mg-1.96Si-0.75Mn calculated by Pandat software.

4.2. Microstructural formation and evolution

The unique microstructures are formed in the as-LPBFed Al5Mg3Zn2Si alloy, as shown in Fig. 6. It is reasonable to expect that the unique microstructures are highly related to the high cooling rates (as high as $\sim 10^6$ K/s) and thermal gradients during solidification process in LPBF process. The Al-Mg$_2$Si eutectic phases show columnar and cellular morphology on longitudinal section with ultrafine sizes. The formation of fine zones, coarse zones and HAZ at melt pool boundary can be roughly summarised as two possible reasons. (1) The undercooling across the melt pool changes due to the Gauss distribution of the laser energy. This can result in the variation of temperature gradient (G) and solidification rate (R), which have synergistic effects on the growth of grains [63]. The values of $G \times R$ determine the grain structure [4]. Therefore, the coarse grain zones are formed at the melt boundary because the low values of $G \times R$ produce coarser grain structures. In reality, the variation of $G \times R$ is continuous across the melt

pool, the microstructure is refined gradually across the melt pool. (2) The size of coarse grains grows continuously due to the remelting of solidified phase. There may exist a secondary solidification or recrystallisation during processing.

It needs to emphasize that the formation of GP zones may be associated with natural ageing in the experimental alloy because Zn content is high. This phenomenon can be enhanced in the super saturation of solute solution induced by high cooling rates during solidification in LPBF process. However, this is a complex process and may involve in several sophisticate mechanisms, so it needs a special investigation in this topic and corresponding systematically research will be presented in the near future. More importantly, it is surprisingly found that GP zones are located inside α-Al grains, together with the rod-shaped $MgZn_2$ precipitates. Meanwhile, all of them have excellent coherent relationship with α-Al. The multiple scales of GP zones and $MgZn_2$ phases may play an important role for precipitates strengthening.

4.3. Mechanisms for improving mechanical properties

In the as-LPBFed Al5Mg3Zn2Si alloy, the exceptional mechanical properties were achieved with the UTS of 548 MPa, the YS of 403 MPa and the El of 6.7%. In general, the improvement in strength results from the restriction of dislocation movement, in which four sources of dislocation movement obstruction are available in the experimental alloy processed by LPBF, including solid solution strengthening, grain boundary strengthening, dispersoid strengthening and precipitates strengthening.

The solubility of Mg, Si and Zn solutes in Al is closely associated with the cooling rate. Particularly, the maximum solubility of Zn in Al is 0.85% under ambient condition. However, the high cooling rate can increase the solute concentration in Al matrix due to the high solubility of Zn in Al alloy at high temperatures. For examples, the solubility of Zn in Al is 67% at 381℃, which is the highest one among all the elements [64]. The significant content of Zn in Al matrix result in supersaturated solid solutions. Thus, the solutes induce lattice distortion due to the difference in atomic sizes, which strongly hinder the dislocation movement and improve the strength. Meanwhile, the addition of Zn to the Al-5Mg-2Si alloy promotes the formation of very fine fully coherent GP zones and $MgZn_2$ phases during LPBF solidification, as shown in Figs. 8&9. Generally, the GP zones and $MgZn_2$ phase can obviously improve strength properties, as coherent fine precipitates are easily sheared by moving dislocations during deformation [65, 66]. Compared with previous Al-5Mg-2Si alloy, the LPBFed Al5Mg3Zn2Si alloy showed

a higher yield strength about 108MPa. It is indicated that the improved YS from Zn addition was mainly due to the Orowan strengthening of the GP zones, MgZn$_2$ phases. The increment of YS caused by Orowan strengthening can be expressed as Eq.1 and Eq.2 [67-69]:

$$\sigma_{Or} = \frac{0.4MGb}{\pi(1-v)^{\frac{1}{2}}}\frac{In(d/b)}{\lambda} \tag{1}$$

$$\lambda = \frac{1}{2}d\sqrt{3\pi/2f_v} \tag{2}$$

where b is Burger vector, v is the Poisson's ratio, G is the shear modulus of the matrix, and d is the average diameter of the particle, λ is the inter-spacing between precipitates in the glide plane, which is linked with the diameter d and volume fraction f_v of the precipitate M is Taylor factor. The values of parameters in Eq.1 and Eq.2 are listed in Tab. S1. In this section, the Orowan strengthening from MgZn$_2$ and GP zones were calculated for evaluating the strengthening effect of adding Zn in the as-LPBFed Al5Mg3Zn2Si alloy. The Orowan strengthening for fine GP zones with an average radius of 6.3 nm and volume fraction of 1.1% was calculated as 106 MPa. Moreover, the mean radius (14.6 nm) and volume fraction (3.2%) of the MgZn$_2$ led to an estimated precipitation strengthening of 95 MPa. Meanwhile, it is noted that formation of GP zones and MgZn$_2$ precipitates will consume solute Mg (~1.5wt.%) in the eutectic Al (since 2wt% Si will consume 3.5 wt.% Mg to form Mg$_2$Si eutectics). The loss of solute solution strengthening should be taken into account. And yield strength is related to the solid solution effect by [70]:

$$\sigma_{SS} = \sum_i k_i c_i{}^{2/3}, (i = \text{Mg}) \tag{3}$$

where c_i is the concentration of I solute (in wt.%) and k_i is a scaling factor for the i solute: $k_{Mg} \approx 29.0$ MPa (wt.%)$^{-2/3}$ [71]. The strength from Mg (~1.5wt%) is calculated to be 43 MPa. In fact, it is considered that the Orowan strengthening from MgZn$_2$ and GP zones cannot linearly superposed, due to the loss of solute solution strengthening, defects, shape difference and distribution heterogeneity of particles in LPBFed alloy. Therefore, it is probably reasonable that the increased yield strength (~108 MPa) is in the range of 63 ~ 158 MPa.

Moreover, the high cooling rate also restricts the growth of grains during solidification, resulting in the formation of extremely fine grains in the as-fabricated aluminium alloys, as shown in Fig.6. Numerous fine and equiaxed grains can be formed in LPBFed alloys. Grain boundaries are excellent in capturing dislocations and therefore the existence of

grain boundaries is the main resources to hinder the movement of dislocations and to induce strengthening. Similarly, nano-sized Mg_2Si, α-Al(Fe,Mn)Si phases are uniformly distributed in Al matrix, these nanophases have very low misfit to the matrix, so it may contribute extraordinarily for strengthening in the as-fabricated alloys. It is known that the precipitated particles can promote the dislocation bowing because of the coherent interfaces between precipitates and α-Al, which also provide the enhancement caused by Orowan mechanism. In a nutshell, multiple strengthening mechanisms work synergically in the as-LPBFed Al5Mg3Zn2Si alloy, resulting in superb mechanical properties. The current work also paves a new way in alloy design for additive manufacturing to achieve remarkable precipitate strengthening without conventional post-fabrication ageing at elevated temperatures because the intrinsic thermal cycles during the LPBF process could deliver sufficient thermal activation for precipitation from the super-saturated solid solution that forms at the initial high cooling rates.

5. Conclusions

In the present study, we investigated the Al5Mg3Zn2Si alloy using laser powder bed fusion (LPBF) for process optimisation, microstructural characteristics and mechanical properties under as-LPBFed condition. The main conclusions can be drawn as follows:

(1) The as-LPBFed Al5Mg3Zn2Si alloy can offer excellent mechanical properties, in which the ultimate tensile strength is 548 MP a, the yield strength is 403 MPa, and the elongation is 6.7%. The superior strength can be attributed to the enhancement in strengthening mechanisms including solid solution strengthening, grain boundary strengthening, dispersoid strengthening and precipitates strengthening.

(2) The highest relative density of 98.9% can be obtained at VED 129.1 J/mm^3 in the as-LPBFed Al5Mg3Zn2Si alloy. The excellent formability of the alloy can be mainly attributed to the numerous fine Al-Mg_2Si eutectics to mitigate hot-cracking. Also, the fine equiaxed grain structure induced by the process parameters can avoid the formation of cracking.

(3) The as-LPBFed microstructure in the Al5Mg3Zn2Si alloy is featured by fine and equiaxed α-Al grains and relatively coarse columnar α-Al grains. The mean size of grains is 13.1 μm in the horizontal section, and 14.4 μm in the longitudinal section.

(4) Typical cellular microstructures consist of Mg_2Si eutectic and α-Al phase formed under high cooling rate during solidification. The coherent α-Al(Fe,Mn)Si and

MgZn$_2$ nanoparticles are formed around the cells. Moreover, the high density plate-shaped GP zones are precipitated inside the cellular eutectic with the size of 20-30 nm long and about 3 nm wide.

CRediT authorship contribution statement

Feipeng Yang: Data curation, Writing - original draft, Investigation. **Jianying Wang:** Investigation, Writing - review. **Tao Wen:** Investigation. **Lei Zhang:** Conceptualization, Supervision. **Xixi Dong:** Conceptualization, Writing - review &editing, Supervision. **Dong Qiu:** Conceptualization, Writing - review & editing, Supervision. **Hailin Yang:** Conceptualization, Funding acquisition, Project, administration, Writing - review & editing, Supervision. **Shouxun Ji:** Conceptualization, Results review, Writing - review.

Declaration of Competing Interest

The authors declare that they have no known competing financial interests or personal relationships that could have appeared to influence the work reported in this paper.

References

[1] E. Georgantzia, M. Gkantou, G.S. Kamaris, Aluminium alloys as structural material: A review of research, Eng. Struct. 227 (2021) 111372, https://doi.org/10.1016/j.engstruct.2020.111372.

[2] D. Herzog, V. Seyda, E. Wycisk, C. Emmelmann, Additive manufacturing of metals, Acta Mater. 117 (2016) 371-392, https://doi.org/10.1016/j.actamat.2016.07.019.

[3] B. Blakey-Milner, P. Gradl, G. Snedden, M. Brooks, J. Pitot, E. Lopez, M. Leary, F. Berto, A. du Plessis, Metal additive manufacturing in aerospace: A review, Mater. Des. 209 (2021) 110008, https://doi.org/10.1016/j.matdes.2021.110008.

[4] H.R. Kotadia, G. Gibbons, A. Das, P.D. Howes, A review of Laser Powder Bed Fusion Additive Manufacturing of aluminium alloys: Microstructure and properties, Addit. Manuf. 46 (2021) 102155, https://doi.org/10.1016/j.addma.2021.102155.

[5] N. Takata, M. Liu, H. Kodaira, A. Suzuki, M. Kobashi, Anomalous strengthening by supersaturated solid solutions of selectively laser melted Al–Si-based alloys, Addit. Manuf. 33 (2020) 101152, https://doi.org/10.1016/j.addma.2020.101152.

[6] J.R. Croteau, S. Griffiths, M.D. Rossell, C. Leinenbach, C. Kenel, V. Jansen, D.N.

Seidman, D.C. Dunand, N.Q. Vo, Microstructure and mechanical properties of Al-Mg-Zr alloys processed by selective laser melting, Acta Mater. 153 (2018) 35-44, https://doi.org/10.1016/j.actamat.2018.04.053.

[7] N.T. Aboulkhair, M. Simonelli, L. Parry, I. Ashcroft, C. Tuck, R. Hague, 3D printing of Aluminium alloys: Additive Manufacturing of Aluminium alloys using selective laser melting, Prog. Mater. Sci. 106 (2019) 100578, https://doi.org/10.1016/j.pmatsci.2019.100578.

[8] J.H. Martin, B.D. Yahata, J.M. Hundley, J.A. Mayer, T.A. Schaedler, T.M. Pollock, 3D printing of high-strength aluminium alloys, Nature. 549 (2017) 365-369, https://doi.org/10.1038/nature23894.

[9] Q. Jia, P. Rometsch, P. Kürnsteiner, Q. Chao, A. Huang, M. Weyland, L. Bourgeois, X. Wu, Selective laser melting of a high strength Al-Mn-Sc alloy: Alloy design and strengthening mechanisms, Acta Mater. 171 (2019) 108-118, https://doi.org/10.1016/j.actamat.2019.04.014.

[10] Y. Qi, H. Zhang, X. Nie, Z. Hu, H. Zhu, X. Zeng, A high strength Al–Li alloy produced by laser powder bed fusion: Densification, microstructure, and mechanical properties, Addit. Manuf. 35 (2020) 101346, https://doi.org/10.1016/j.addma.2020.101346.

[11] H. Zhang, H. Zhu, X. Nie, J. Yin, Z. Hu, X. Zeng, Effect of Zirconium addition on crack, microstructure and mechanical behavior of selective laser melted Al-Cu-Mg alloy, Scr. Mater. 134 (2017) 6-10, https://doi.org/10.1016/j.scriptamat.2017.02.036.

[12] Z. Wang, X. Lin, N. Kang, Y. Hu, J. Chen, W. Huang, Strength-ductility synergy of selective laser melted Al-Mg-Sc-Zr alloy with a heterogeneous grain structure, Addit. Manuf. 34 (2020) 101260, https://doi.org/10.1016/j.addma.2020.101260.

[13] R. Li, M. Wang, Z. Li, P. Cao, T. Yuan, H. Zhu, Developing a high-strength Al-Mg-Si-Sc-Zr alloy for selective laser melting: Crack-inhibiting and multiple strengthening mechanisms, Acta Mater. 193 (2020) 83-98, https://doi.org/10.1016/j.actamat.2020.03.060.

[14] J. Bi, Z. Lei, Y. Chen, X. Chen, Z. Tian, J. Liang, X. Qin, X. Zhang, Densification, microstructure and mechanical properties of an Al-14.1Mg-0.47Si-0.31Sc-0.17Zr alloy printed by selective laser melting, Mater. Sci. Eng. A 774 (2020) 138931, https://doi.org/10.1016/j.msea.2020.138931.

[15] Z. Zhu, F.L. Ng, H.L. Seet, W. Lu, C.H. Liebscher, Z. Rao, D. Raabe, S. Mui Ling Nai, Superior mechanical properties of a selective-laser-melted AlZnMgCuScZr alloy enabled by a tunable hierarchical microstructure and dual-nanoprecipitation, Mater.

Today. (2021), https://doi.org/10.1016/j.mattod.2021.11.019.

[16] X. Li, D. Li, G. Li, Q. Cai, Microstructure, mechanical properties, aging behavior, and corrosion resistance of a laser powder bed fusion fabricated Al–Zn–Mg–Cu–Ta alloy, Mater. Sci. Eng. A 832 (2022) 142364, https://doi.org/10.1016/j.msea.2021.142364.

[17] F. Xiao, S. Wang, Y. Wang, D. Shu, G. Zhu, B. Sun, D. StJohn, Niobium nanoparticle-enabled grain refinement of a crack-free high strength Al-Zn-Mg-Cu alloy manufactured by selective laser melting, J. Alloy. Compd. 900 (2022) 163427, https://doi.org/10.1016/j.jallcom.2021.163427.

[18] H. Yang, Y. Zhang, J. Wang, Z. Liu, C. Liu, S. Ji, Additive manufacturing of a high strength Al-5Mg2Si-2Mg alloy: Microstructure and mechanical properties, J. Mater. Sci. Tech. 91 (2021) 215-223, https://doi.org/10.1016/j.jmst.2021.02.048.

[19] J. Deng, C. Chen, X. Liu, Y. Li, K. Zhou, S. Guo, A high-strength heat-resistant Al−5.7Ni eutectic alloy with spherical Al3Ni nano-particles by selective laser melting, Scr. Mater. 203 (2021) 114034, https://doi.org/10.1016/j.scriptamat.2021.114034.

[20] W. Wang, N. Takata, A. Suzuki, M. Kobashi, M. Kato, High-temperature strength sustained by nano-sized eutectic structure of Al–Fe alloy manufactured by laser powder bed fusion, Mater. Sci. Eng. A 838 (2022) 142782, https://doi.org/10.1016/j.msea.2022.142782.

[21] K. Sisco, A. Plotkowski, Y. Yang, D. Leonard, B. Stump, P. Nandwana, R.R. Dehoff, S.S. Babu, Microstructure and properties of additively manufactured Al-Ce-Mg alloys, Sci. Rep. 11(1) (2021) 6953, https://doi.org/10.1038/s41598-021-86370-4.

[22] A. Plotkowski, K. Sisco, S. Bahl, A. Shyam, Y. Yang, L. Allard, P. Nandwana, A.M. Rossy, R.R. Dehoff, Microstructure and properties of a high temperature Al–Ce–Mn alloy produced by additive manufacturing, Acta Mater. 196 (2020) 595-608, https://doi.org/10.1016/j.actamat.2020.07.014.

[23] A. Mehta, L. Zhou, T. Huynh, S. Park, H. Hyer, S. Song, Y. Bai, D.D. Imholte, N.E. Woolstenhulme, D.M. Wachs, Y. Sohn, Additive manufacturing and mechanical properties of the dense and crack free Zr-modified aluminum alloy 6061 fabricated by the laser-powder bed fusion, Addit. Manuf. 41 (2021) 101966, https://doi.org/10.1016/j.addma.2021.101966.

[24] S.Z. Uddin, L.E. Murr, C.A. Terrazas, P. Morton, D.A. Roberson, R.B. Wicker, Processing and characterization of crack-free aluminum 6061 using high-temperature heating in laser powder bed fusion additive manufacturing, Addit. Manuf. 22 (2018) 405-415, https://doi.org/10.1016/j.addma.2018.05.047.

[25] K.G. Prashanth, S. Scudino, T. Maity, J. Das, J. Eckert, Is the energy density a reliable parameter for materials synthesis by selective laser melting, Mater. Res. Lett. 5(6) (2017) 386-390, https://doi.org/10.1080/21663831.2017.1299808.

[26] Y.K. Xiao, Z.Y. Bian, Y. Wu, G. Ji, Y.Q. Li, M.J. Li, Q. Lian, Z. Chen, A. Addad, H.W. Wang, Effect of nano-TiB$_2$ particles on the anisotropy in an AlSi10Mg alloy processed by selective laser melting, J. Alloy. Compd. 798 (2019) 644-655. https://doi.org/10.1016/j.jallcom.2019.05.279.

[27] L. Zhou, A. Mehta, E. Schulz, B. McWilliams, K. Cho, Y. Sohn, Microstructure, precipitates and hardness of selectively laser melted AlSi10Mg alloy before and after heat treatment, Mater. Char. 143 (2018) 5-17. https://doi.org/10.1016/j.matchar.2018.04.022.

[28] J. Bi, Z.L. Lei, Y.B. Chen, X. Chen, N.N. Lu, Z. Tian, X.K. Qin, An additively manufactured Al-14.1Mg-0.47Si-0.31Sc-0.17Zr alloy with high specific strength, good thermal stability and excellent corrosion resistance, J. Mater. Sci. Tech. 67 (2021) 23-35. https://doi.org/10.1016/j.jmst.2020.06.036.

[29] A.K. Syed, B. Ahmad, H. Guo, T. Machry, D. Eatock, J. Meyer, M.E. Fitzpatrick, X. Zhang, An experimental study of residual stress and direction-dependence of fatigue crack growth behavior in as-built and stress-relieved selective-laser melted Ti6Al4V, Mater. Sci. Eng. A 755 (2019) 246–257. https://doi.org/10.1016/j.msea.2019.04.023.

[30] A. Wang, Y. Yan, Z. Chen, H. Qi, Y. Yin, X. Wu, Q. Jia, Characterisation of the multiple effects of Sc/Zr elements in selective laser melted Al alloy, Mater. Charact. 183 (2022) 111653, https://doi.org/10.1016/j.matchar.2021.111653.

[31] X. Zhu, H. Yang, X. Dong, S. Ji, The effects of varying Mg and Si levels on the microstructural inhomogeneity and eutectic Mg$_2$Si morphology in die-cast Al–Mg–Si alloys, J. Mater. Sci. 54 (7) (2018) 5773-5787, https://doi.org/10.1007/s10853-018-03198-6.

[32] H. Zhang, Y. Wang, J.J. Wang, D.R. Ni, D. Wang, B.L. Xiao, Z.Y. Ma, Achieving superior mechanical properties of selective laser melted AlSi10Mg via direct aging treatment, J. Mater. Sci. Tech. 108 (2022) 226-235, https://doi.org/10.1016/j.jmst.2021.07.059.

[33] B. Zhang, W. Wei, W. Shi, Y.W. Guo, S.P. Wen, X.L. Wu, K.Y. Gao, L. Rong, H. Huang, Z.R. Nie, Effect of heat treatment on the microstructure and mechanical properties of Er-containing Al–7Si–0.6 Mg alloy by laser powder bed fusion, J. Mater. Res. Technol. 18 (2022) 3073-3084. https://doi.org/10.1016/j.jmrt.2022.04.023.

[34] P. Li, Y. Kim, A.C. Bobel, L.G. HectorJr, A.K. Sachde, S. Kumar, A.F. Bowe,

Microstructural origin of the anisotropic flow stress of laser powder bed fused AlSi10Mg, Acta Mater. 220 (2021) 117346. https://doi.org/10.1016/j.actamat.2021.117346.

[35] W. Li, S. Li, J. Liu, A. Zhang, Y. Zhou, Q. Wei, C. Yan, Y. Shi, Effect of heat treatment on AlSi10Mg alloy fabricated by selective laser melting: Microstructure evolution, mechanical properties and fracture mechanism, Mater. Sci. Eng. A 663 (2016) 116-125. https://doi.org/10.1016/j.msea.2016.03.088

[36] B. Liu, D. Raabe, P. Eisenlohr, F. Roters, A. Arsenlis, G. Hommes, Dislocation interactions and low-angle grain boundary strengthening, Acta Mater. 59(19) (2011) 7125-7134, https://doi.org/10.1016/j.actamat.2011.07.067.

[37] K. Lu, L. Lu, S. Suresh, Strengthening materials by engineering coherent internal boundaries at the nanoscale, Science. 324(5925) (2009) 349-352, https://doi.org/10.1126/science.1159610.

[38] X.J. Wang, L.C. Zhang, M.H. Fang, T.B. Sercombe, The effect of atmosphere on the structure and properties of a selective laser melted Al–12Si alloy, Mater. Sci. Eng. A 597 (2014) 370-375, https://doi.org/10.1016/j.msea.2014.01.012.

[39] M. Wang, B. Song, Q. Wei, Y. Zhang, Y. Shi, Effects of annealing on the microstructure and mechanical properties of selective laser melted AlSi7Mg alloy, Mater. Sci. Eng. A 739 (2019) 463-472, https://doi.org/10.1016/j.msea.2018.10.047.

[40] J.H. Rao, Y. Zhang, X. Fang, Y. Chen, X. Wu, C.H.J. Davies, The origins for tensile properties of selective laser melted aluminium alloy A357, Addit. Manuf. 17 (2017) 113-122, https://doi.org/10.1016/j.addma.2017.08.007.

[41] K.G. Prashanth, S. Scudino, J. Eckert, Defining the tensile properties of Al-12Si parts produced by selective laser melting, Acta Mater. 126 (2017) 25-35, https://doi.org/10.1016/j.actamat.2016.12.044.

[42] B. Chen, S.K. Moon, X. Yao, G. Bi, J. Shen, J. Umeda, K. Kondoh, Strength and strain hardening of a selective laser melted AlSi10Mg alloy, Scr. Mater. 141 (2017) 45-49, https://doi.org/10.1016/j.scriptamat.2017.07.025.

[43] J.H. Rao, Y. Zhang, K. Zhang, X. Wu, A. Huang, Selective laser melted Al-7Si-0.6Mg alloy with in-situ precipitation via platform heating for residual strain removal, Mater. Des. 182 (2019) 108005, https://doi.org/10.1016/j.matdes.2019.108005.

[44] T. Kimura, T. Nakamoto, Microstructures and mechanical properties of A356 (AlSi7Mg0.3) aluminum alloy fabricated by selective laser melting, Mater. Des. 89 (2016) 1294-1301, https://doi.org/10.1016/j.matdes.2015.10.065.

[45] Y. Bai, Y. Yang, Z. Xiao, M. Zhang, D. Wang, Process optimization and mechanical

property evolution of AlSiMg0.75 by selective laser melting, Mater. Des. 140 (2018) 257-266, https://doi.org/10.1016/j.matdes.2017.11.045.

[46] L. Hitzler, C. Janousch, J. Schanz, M. Merkel, B. Heine, F. Mack, W. Hall, A. Öchsner, Direction and location dependency of selective laser melted AlSi10Mg specimens, J. Mater. Process. Tech. 243 (2017) 48-61, https://doi.org/10.1016/j.jmatprotec.2016.11.029.

[47] I. Rosenthal, A. Stern, N. Frage, Strain rate sensitivity and fracture mechanism of AlSi10Mg parts produced by Selective Laser Melting, Mater, Sci. Eng. A 682 (2017) 509-517, https://doi.org/10.1016/j.msea.2016.11.070.

[48] L. Li, R. Li, T. Yuan, C. Chen, Z. Zhang, X. Li, Microstructures and tensile properties of a selective laser melted Al–Zn–Mg–Cu (Al7075) alloy by Si and Zr microalloying, Mater. Sci. Eng. A 787 (2020) 139492, https://doi.org/10.1016/j.msea.2020.139492.

[49] L. Li, R. Li, T. Yuan, C. Chen, M. Wang, J. Yuan, Q. Weng, Microstructures and mechanical properties of Si and Zr modified Al–Zn–Mg–Cu alloy-A comparison between selective laser melting and spark plasma sintering, J. Alloy. Compd. 821 (2020) 153520, https://doi.org/10.1016/j.jallcom.2019.153520.

[50] S. Ji, D. Watson, Z. Fan, M. White, Development of a super ductile diecast Al–Mg–Si alloy, Mater. Sci. Eng. A 556 (2012) 824-833, https://doi.org/10.1016/j.msea.2012.07.074.

[51] Z. Hu, L. Wan, S. Wu, H. Wu, X. Liu, Microstructure and mechanical properties of high strength die-casting Al–Mg–Si–Mn alloy, Mater. Des. 46 (2013) 451-456, https://doi.org/10.1016/j.matdes.2012.10.020.

[52] C. He, Y. Li, J. Li, G. Xu, Z. Wang, D. Wu, Effect of electromagnetic fields on microstructure and mechanical properties of sub-rapid solidification-processed Al–Mg–Si alloy during twin-roll casting, Mater. Sci. Eng. A 766 (2019) 138328, https://doi.org/10.1016/j.msea.2019.138328.

[53] O. Prach, O. Trudonoshyn, P. Randelzhofer, C. Körner, K. Durst, Effect of Zr, Cr and Sc on the Al–Mg–Si–Mn high-pressure die casting alloys, Mater. Sci. Eng. A 759 (2019) 603-612, https://doi.org/10.1016/j.msea.2019.05.038.

[54] L. Li, S. Ji, Q. Zhu, Y. Wang, X. Dong, W. Yang, S. Midson, Y. Kang, Effect of Zn Concentration on the Microstructure and Mechanical Properties of Al-Mg-Si-Zn Alloys Processed by Gravity Die Casting, Metall. Mater. Trans. A 49(8) (2018) 3247-3256, https://doi.org/10.1007/s11661-018-4684-2.

[55] O. Trudonoshyn, S. Rehm, P. Randelzhofer, C. Körner, Improvement of the high-

pressure die casting alloy Al-5.7Mg-2.6Si-0.7Mn with Zn addition, Mater. Charact. 158 (2019) 109959, https://doi.org/10.1016/j.matchar.2019.109959.

[56] S.X. Ji, D. Watson, Y. Wang, M. White, Z.Y. Fan, Effect of Ti Addition on Mechanical Properties of High Pressure Die Cast Al-Mg-Si Alloys, Mater. Sci. Forum. 765 (2013) 23-27, https://doi.org/10.4028/www.scientific.net/MSF.765.23.

[57] Y. Pan, D. Zhang, H. Liu, Z. Zhang, H. Li, L. Zhuang, J. Zhang, Reducing welding hot cracking of high-strength novel Al–Mg–Zn–Cu alloys based on the prediction of the T-shaped device, Sci. Technol. Weld. Joi. 25(6) (2020) 483-489. https://doi.org/10.1080/13621718.2020.1746035

[58] J. Liu, P. Zeng, S. Kou, Solidification cracking susceptibility of quaternary aluminium alloys, Sci. Technol. Weld. Joi. 26(3) (2021) 244-257. https://doi.org/10.1080/13621718.2021.1893007

[59] J.D. Robson, D.T. Henry, B. Davis, Particle effects on recrystallization in magnesium–manganese alloys: Particle pinning, Mater. Sci. Eng. A 528 (12) (2011) 4239-4247, https://doi.org/10.1016/j.msea.2011.02.030.

[60] Y. Lang, Y. Cai, H. Cui, J. Zhang, Effect of strain-induced precipitation on the low angle grain boundary in AA7050 aluminum alloy, Mater. Des. 32 (2011) 4241-4246, https://doi.org/10.1016/j.matdes.2011.04.025.

[61] T. Soysal, S. Kou, A simple test for assessing solidification cracking susceptibility and checking validity of susceptibility prediction, Acta Mater. 143 (2018) 181-197, https://doi.org/10.1016/j.actamat.2017.09.065.

[62] P. Gao, W. Huang, H. Yang, G. Jing, Q. Liu, G. Wang, Z. Wang, X. Zeng, Cracking behavior and control of β-solidifying Ti-40Al-9V-0.5Y alloy produced by selective laser melting, J. Mater. Sci. Tech. 39 (2020) 144-154, https://doi.org/10.1016/j.jmst.2019.08.026.

[63] X. Liu, C. Zhao, X. Zhou, Z. Shen, W. Liu, Microstructure of selective laser melted AlSi10Mg alloy, Mater. Des. 168 (2019) 107677, https://doi.org/10.1016/j.matdes.2019.107677.

[64] Z. Skoko, S. Popović, G. Štefanić, Microstructure of Al-Zn and Zn-Al Alloys, Croat. Chem. Acta. 82 (2009) 405-420, https://hrcak.srce.hr/39658.

[65] S.-H. Lee, J.-G. Jung, S.-I. Baik, D.N. Seidman, M.-S. Kim, Y.-K. Lee, K. Euh, Precipitation strengthening in naturally aged Al–Zn–Mg–Cu alloy, Mater. Sci. Eng. A 803 (2021) 140719, https://doi.org/10.1016/j.msea.2020.140719.

[66] J. Zhao, Z. Liu, S. Bai, D. Zeng, L. Luo, J. Wang, Effects of natural aging on the formation and strengthening effect of G.P. zones in a retrogression and re-aged Al–Zn–

Mg–Cu alloy, J. Alloy. Compd. 829 (2020) 154469, https://doi.org/10.1016/j.jallcom.2020.154469.

[67] Z. Hu, H. Zhang, H. Zhu, Z. Xiao, X. Nie, X. Zeng, Microstructure, mechanical properties and strengthening mechanisms of AlCu5MnCdVA aluminum alloy fabricated by selective laser melting, Mater. Sci. Eng. A 759 (2019) 154-166, https://doi.org/10..1016/j.msea.2019.04.114.

[68] K. Ma, H. Wen, T. Hu, T.D. Topping, D. Isheim, D.N. Seidman, E.J. Lavernia, J.M. Schoenung, Mechanical behavior and strengthening mechanisms in ultrafine grain precipitation-strengthened aluminum alloy, Acta Mater. 62 (2014) 141-155, https://doi.org/10.1016/j.actamat.2013.09.042.

[69] A.J. Ardell, Precipitation hardening, Metall. Trans. A, 16 (1985) 2141−2165, https://doi.org/10.1007/BF02670416.

[70] S.P. Yuan, G. Liu, R.H. Wang, X. Pu, G.J. Zhang, J. Sun, K.H. Chen, Coupling effect of multiple precipitates on the ductile fracture of aged Al–Mg–Si alloys, Scr. Mater. 57 (9) (2007) 865-868, https://doi.org/10.1016/j.scriptamat.2007.06.063.

[71] O.R. Myhr, Ø. Grong, S.J. Andersen, Modelling of the age hardening behaviour of Al–Mg–Si alloys, Acta Mater. 49 (2001) 65–75, https://doi.org/10.1016/S1359-6454(00)00301-3.